Original article

Estimation-based model predictive control of an electrically-heated steam methane reforming process

Xiaodong Cui [a], Berkay Çıtmacı [a], Dominic Peters [a], Fahim Abdullah [a], Yifei Wang [a], Esther Hsu [a], Parth Chheda [a], Carlos G. Morales-Guio [a], Panagiotis D. Christofides [a,b,*]

[a] Department of Chemical and Biomolecular Engineering, University of California, Los Angeles, CA, 90095-1592, USA
[b] Department of Electrical and Computer Engineering, University of California, Los Angeles, CA 90095-1592, USA

ARTICLE INFO

ABSTRACT

The surge in demand for hydrogen (H_2) across diverse sectors, including clean energy transportation and chemical synthesis, underscores the need for a thorough investigation into H_2 production dynamics and the development of effective controllers for industrial applications. This paper focuses on an electrically heated steam methane reforming (SMR) process for H_2 production, offering advantages such as enhanced environmental sustainability, compactness, efficiency, and controllability compared to conventional reforming methods. Electric heating of the entire system allows for adjustments in current to control reactor temperature, thereby impacting hydrogen production rates. However, accurately modeling hydrogen production dynamics presents a formidable challenge, as complex models with high precision are computationally unsuitable for real-time control integration. Considering these factors, an accurate and efficient first-principles-based lumped-parameter model is developed to provide a dependable estimation of hydrogen production in an electrically-heated steam methane reformer. This model is validated experimentally and then utilized in a model predictive controller (MPC). To obtain the necessary state estimate information for the MPC, an extended Luenberger observer (ELO) method is employed to estimate state variables from limited, infrequent and delayed measurements of gas-phase reactor outlet stream and frequent measurements of the reactor temperature. Simulation comparisons with a proportional-integral (PI) controller reveal a much faster response in achieving the desired H_2 production rate under the estimation-based MPC. Additionally, the simulations demonstrate the robustness of the controller to process variability such as a decrease in catalyst activation energy, commonly encountered in the SMR process, highlighting its effectiveness in maintaining stable operation under varying process conditions.

1. Introduction

In recent decades, there has been a significant increase in demand for hydrogen (H_2) due to its extensive utilization across various fields. In transportation, H_2-fueled vehicles exhibit superior performance for long-distance driving when compared to battery-powered vehicles (Yue et al., 2021). In chemical synthesis, H_2 is utilized at major industrial scales as a reactant for synthesizing chemicals like ammonia (NH_3) and methanol (CH_3OH) (Siddiqui et al., 2020; Bowker, 2019; Ramachandran and Menon, 1998). The increasing need for hydrogen has motivated extensive efforts for the production of hydrogen through environmentally-friendly routes like water electrolysis. However, at this point, the production of green hydrogen in a large-scale by water electrolysis as well as other methods is limited, and the most commonly used hydrogen production method continues to be steam methane reforming (SMR) (Holladay et al., 2009; Uddin et al., 2020).

In SMR, the traditional heat source to drive the reforming reactions and produce the hydrogen is the combustion of hydrocarbons (Wismann et al., 2019), leading to the emission of substantial CO_2. Additionally, in conventional SMR setups, energy is transferred through radiation from a high temperature flame. Conventional SMR heating requires significant reactor volumes to minimize shadowing and to allow enough distance to prevent reactor coils from exceeding their temperature limits. The large reactor volumes necessitated by conventional SMR setups lead to large plant footprints (Wismann et al., 2019), and introduce temperature gradients on the reaction coils. The radiant section of a conventional SMR furnace is a heat transfer-limited process that limits heat fluxes to around 80 kW per square meter of coil surface (Häussinger et al., 2011), resulting in low energy efficiency. Hence, in the present work, an electrically-heated SMR system is introduced and investigated as a novel method for H_2 production.

Electrification can replace the combustion-based heating system, resulting in a significantly smaller required reformer volume (Wismann et al., 2019). Moreover, utilizing renewable electricity can result in near zero-carbon emissions, thereby posing substantially reduced effects on the environment. To make this novel SMR approach implementable in an H_2 production industrial setting, a thorough study of the dynamic behavior of H_2 production and the design of controllers to ensure optimal and stable production rates becomes essential.

In studying the dynamic behavior, extensive efforts have focused on varying parameters such as temperature, pressure, and catalyst activity to understand their impact on the process. For example, El-Bousiffi and Gunn (2007) dynamically studied the impact of the temperature change from 600 to 840 °C and the pressure change from 2.5 to 9 atm for the experiment. However, many factors make it hard to quantitatively build a model to capture this dynamic behavior. First, all reactants and products are in gas phase, meaning that the volumetric flowrate is not constant and should be quantified. Additionally, since SMR reactions are catalytic, mass transfer phenomena should be considered. Also, since tubular flow reactors are employed for SMR reactions, the varying profiles across the axial direction should be taken into account. Therefore, many of these models utilize a combination of tubular reactor mole balance and computational fluid dynamics (CFD) to accurately capture the complex dynamics of the system (Mokheimer et al., 2015; Lao et al., 2016; Tran et al., 2017; Abbas et al., 2017). While these complicated models can capture dynamic behavior relatively accurately, their long computational times render them unsuitable as models for real-time model-based controllers. Therefore, an accurate and time-efficient model is required.

In controller design, numerous advanced model-based control strategies have emerged during the last several decades. Specifically, model predictive control (MPC) has received considerable attention by researchers and been widely employed in manufacturing and process industries. Over the past four decades, stability, performance and robustness issues of MPC have been studied and demonstrated mathematically and practically, contributing to the maturity and usefulness of this control technique (see, for example, Christofides et al., 2013; Ellis et al., 2014 for reviews of results in this area). In the closed-loop implementation of MPC, the measurement feedback from the real process is essential, serving as the initial condition required for the MPC process model to start integrating from. Utilizing this information, MPC predicts the future behavior of the process to determine the optimal control input. Hence, the initial condition from the measurement is crucial for the MPC. However, obtaining measurements of certain quantities in industrial settings is often challenging due to the difficulty of detecting the associated physical parameters or the high cost of sensors. Furthermore, while certain physical parameters are measurable, the protracted duration required for their analysis often results in infrequent and delayed data collection intervals. Nowadays, with the growth of technology, many advanced sensors have been developed and incorporated into the manufacturing instrumentation. However, challenges persist in detecting certain physical quantities, as well as dealing with infrequent and delayed measurement situations, which continue to pose various challenges in process industries.

To address this issue, state estimation methods were employed in many theoretical and practical contexts. The state observer (SO) is one widely used framework to estimate the state values (Wang and Gao, 2003). For example, Luenberger built the observer theory and compared it with other state estimation methods (Luenberger, 1966). Han (1995) established a class of nonlinear extended Luenberger state observers. The Kalman filter is also a ubiquitous state estimation method. The stability and the performance of the case with infrequent, delayed measurements were investigated using a variable dimension unscented Kalman filter by Guo and Huang (2015). The fundamental concept of the state estimation method is to estimate all state variables (required information for MPC) from limited measurement data. This

estimation is achieved by considering both simulated behavior from the model and limited, observed measurements.

Based on this concept, a generalized approach can be formulated for implementing MPC for a nonlinear system with sparse, infrequent, and delayed measurement data. Initially, a few physical parameters are captured from the system via sensors. These parameters are then utilized to approximate all the state variables required for MPC using a state estimation technique. Leveraging the estimated state variables and the system model, the control input is computed and subsequently applied by the actuator to the physical system. Throughout this iterative process, the control input can be computed and applied frequently despite the sparse and intermittent nature of sensor measurements. This proposed strategy is applied to control our electrically-heated SMR system. Specifically, to address modeling challenges, a computationally efficient first-principles model of the experimental process is initially developed, building upon previous work (Çıtmacı et al., 2024). This model is further improved and validated through comparison with experimental data. Subsequently, leveraging this validated model, a model predictive control scheme is designed and implemented on the process model. The MPC utilizes limited, infrequent and delayed measurements of gas-phase reactor outlet properties, along with frequent reactor temperature measurements. The performance of the MPC is compared with Proportional-Integral control under both no-disturbance and under-disturbance (resulting from process variability) conditions.

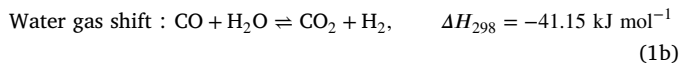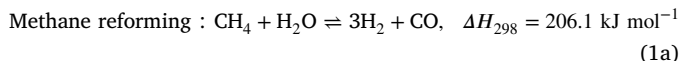## 2. Preliminaries

2.1. Nomenclature

Definitions of variables used in the modeling of the reactor:

- A: Heat transfer area [m^2]
- A_i: Pre-exponential factor of adsorption constant K_i [Pa^{-1} for $i = CH_4, H_2, CO$ and unitless for $i = H_2O$]
- A_j: Pre-exponential factor of rate coefficient k_i [mol $Pa^{0.5}$ (kg − cat s)$^{-1}$ for $j = 1$ (SMR reaction), mol (Pa kg − cat s)$^{-1}$ for $j = 2$ (WGS reaction)]
- C_i: Concentration of gas i [mol m^{-3}]
- C_{p_i}: Heat capacity of gas i [J (mol K)$^{-1}$]
- E_j: Activation energy of reaction j [J mol^{-1}]
- E: Electric potential [V]
- F_T: Outlet total molar flow of gases [mol s^{-1}]
- F_{T0}: Inlet total molar flow of gases [mol s^{-1}]
- F_i: Molar flow of gas i [mol s^{-1}]
- I: Current [A]
- K_i: Adsorption constant of gas i [Pa^{-1} for $i = CH_4, H_2, CO$ and unitless for $i = H_2O$]
- K_j: Equilibrium constant of reaction j [Pa^2 for $j = 1$ (SMR reaction), unitless for $j =2$ (WGS reaction)]
- k_j: Reaction rate constant of reaction j [mol $Pa^{0.5}$ (kg − cat s)$^{-1}$ for $j = 1$ (SMR reaction), mol (Pa kg − cat s)$^{-1}$ for $j = 2$ (WGS reaction)]
- $\dot{m}_{p_i}$: Mass flowrate of gas i [kg s^{-1}]
- P: Total pressure [Pa]
- P_i: Partial pressure of gas i [Pa]
- q: Outlet volumetric flowrate [m^3 s^{-1}]
- r_j: Rate of reaction j [mol (kg s)$^{-1}$]
- R: Universal gas constant [J (mol K)$^{-1}$]
- $\bar{R}$: Heat resistance [Ω]
- T: Reactor temperature [K]
- T_0: Temperature of inlet gas i [K]
- T_s: Ambient temperature [K]
- U: Overall heat transfer coefficient [J (s K m^2)$^{-1}$]
- V_R: Reactor volume [m^3]
- W: Weight of catalyst [kg]

- ΔH_{r_j}: Enthalpy change of reaction j [J mol^{-1}]
- ρ_i: Density of the gas i [kg m^{-3}]

2.2. Process overview

The objective of the SMR process is to generate H$_2$ by the consumption of methane (CH$_4$) and steam, yielding carbon monoxide and carbon dioxide as byproducts. This intricate process involves two primary reactions, the steam methane reforming reaction and the water gas shift (WGS) reaction, as shown in Eq. (1), with each contributing to the overall hydrogen production.

$$\text{Methane reforming}: CH_4 + H_2O \rightleftharpoons 3H_2 + CO, \quad \Delta H_{298} = 206.1 \text{ kJ mol}^{-1} \tag{1a}$$

$$\text{Water gas shift}: CO + H_2O \rightleftharpoons CO_2 + H_2, \quad \Delta H_{298} = -41.15 \text{ kJ mol}^{-1} \tag{1b}$$

The rate-determining step is the reforming reaction due to the difficulty in breaking the C-H bond, making the reforming reaction crucial to increase the rate for this reaction (Wei and Iglesia, 2004a,b,c,d). Therefore, a Ni-ZrO composite catalyst is used to reduce the activation energy of this reaction (Eq. (1a)) since it can help to break the C-H bond in the CH$_4$ molecule.

The reforming reaction is endothermic, and the water gas shift reaction is exothermic, indicating the influence of temperature changes on the equilibrium shift. Consequently, the production rate of H$_2$ can be altered by adjusting the temperature of the entire system. In this experimental work, the joule-heating method is employed to regulate the system's temperature, whereby heat is supplied through electricity, and temperature changes correspond to variations in current. Therefore, manipulating the current can affect the rate of hydrogen production. The quantitative relationship between temperature and current will be further elucidated through an energy balance in Section 4. Based on this, the overall real-time control scheme is built to obtain the desired H$_2$ production by variation of current.

2.3. Extended luenberger observer

The Extended Luenberger Observer (ELO) is a type of state observer to estimate state values from limited measurement information. We do employ an Extended Luenberger observer due to the ease of its design and implementation. To show more details of the algorithm of ELO, a general nonlinear dynamic system is considered of the form:

$$\dot{x} = F(x, u) \tag{2a}$$

$$y = h(x) \tag{2b}$$

where x is the state vector, u is the manipulated input vector, $F(x, u)$ is a nonlinear vector function whose arguments include the state vector and the manipulated input vector, y is the measurement, and $h(x)$ is a nonlinear function that relates the state value to the measurable physical information.

To use the ELO method to estimate the state values, the nonlinear function $F(x, u)$ in dynamic ordinary differential equations (ODEs) is augmented by an observer error term to correct the state values, which is described as in Eq. (3) below:

$$\dot{\hat{x}} = F(\hat{x}, u) + K(y - h(\hat{x})) \tag{3}$$

where $\hat{x}$ represents the estimated state values by ELO, K is the observer gain, and $h(\hat{x})$ is the prediction of the measurable physical information from the state value. The $y - h(\hat{x})$ term represents the error between the measurement and the estimation. To tune the observer gain, the error between the estimated and real state values is introduced ($e = x - \hat{x}$). The derivative of this error is calculated by the following equation (Dochain, 2003):

$$\dot{e} = F(\hat{x} + e, u) - F(\hat{x}, u) - K(h(\hat{x} + e) - h(\hat{x})) \tag{4}$$

Considering this equation, the observer gain (K) should be selected by considering a stability condition for the error linearized system shown below:

$$\dot{e} = (A - KH)e \tag{5}$$

where $A = \frac{\partial F(x,u)}{\partial x}|_{x=x_s}$ and $H = \frac{\partial h(x)}{\partial x}|_{x=x_s}$ are the linearization terms of the nonlinear model around the operating steady-state of the process model. In order to ensure that the estimation error locally (sufficiently close to the operating steady-state) converges to zero, all the eigenvalues of the matrix $A - KH$ should have strictly negative real part.

2.4. Model predictive control

Model predictive control is a widely accepted control strategy in the industry. The central idea is to find the optimal control action by repeatedly solving a minimization problem in real-time by predicting the future process behavior using a model incorporating measurement feedback. While the cost function in optimization is specific to the class of problems being solved, in this problem, we consider a cost function consisting of two terms. The first term represents the error between the target output predicted by the process model and the set-point. The second term represents the penalty on the deviation of the manipulated input from the steady-state value corresponding to the set-point value as calculated by the process model. Mathematically, this minimization problem can be described by the following equations:

$$\mathcal{J} = \min_u \int_{t_k}^{t_{k+N_h}} L(\bar{y}(t), u(t)) \, \mathrm{d}t \tag{6a}$$

$$\text{s.t. } \dot{\bar{x}}(t) = F(\bar{x}(t), u(t)), \ \bar{x}(t_k) = \hat{x}(t_k) \tag{6b}$$

$$\bar{y}(t) = h(\bar{x}(t)) \tag{6c}$$

$$L(\bar{y}(t), u(t)) = A(\bar{y}(t) - y_{sp})^2 + B(u(t) - u_{sp})^2 \tag{6d}$$

$$t \in [t_k, t_{k+N_h}) \tag{6e}$$

$$|u(t_k) - u(t_{k-1})| \leq u_c \tag{6f}$$

$$u(t) \in U \quad \forall t \in (t_k, t_{k+N_h}) \tag{6g}$$

where u is the input control action, $\bar{x}$ is the prediction of the state variables using the model over the horizon, N_h is the horizon length, $F(\bar{x}, u)$ is the model that predicts the state variables, h is the relationship of the state variables and the controlled output, $\bar{y}$ is the controlled output, u_c is the control input change limit, and U is the bound of the manipulated input. A and B represent MPC tuning parameters. Finally, y_{sp} and u_{sp} are the set-point of the target output and the expected control input at the target output, respectively. In the present work, the emphasis is on the development and evaluation of an observer-based MPC scheme that is suitable for experimental implementation (which will be the subject of a following manuscript), and thus, there is no extensive analysis of closed-loop stability properties. In Remark 10 below, we elaborate on this issue.

3. Experimental system and digitalization

In this section, a general introduction to the experimental system and its automation is presented.

3.1. Experimental system overview

The overall experimental system of the electrically-heated steam methane reforming process is illustrated in a process flow diagram in Fig. 1 with its parameters listed in Table 1. Initially, argon, hydrogen, and methane are introduced into the reactor at flowrate values given in Table 2, with their flowrates regulated by flow-meters. These gases are then bubbled into the steam box to create a wet gas mixture.
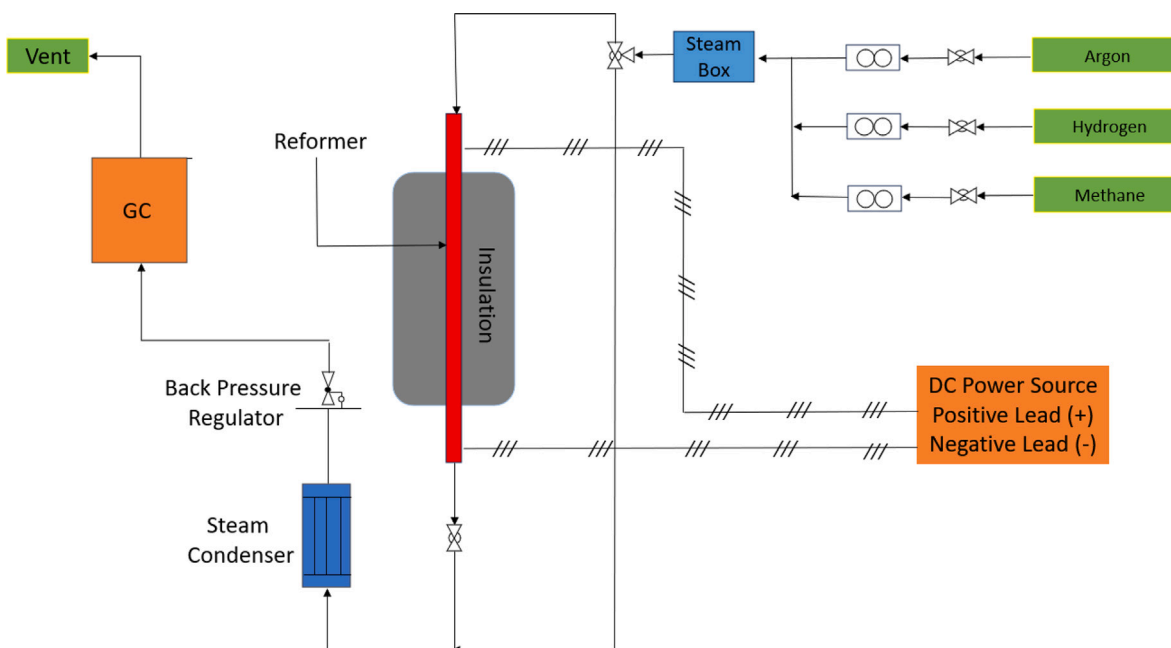
Fig. 1. Process flow diagram of the experimental electrically-heated steam methane reforming process.

Table 1
Experimental system parameters.

T_0 (°C)	T_s (°C)	D (mm)	L (mm)	P (atm)	W (g)	$\bar{R}(\Omega)$
150	25	5.2	500	1	0.05	0.096

Table 2
Experimental inlet flowrates.

F_{CH_4} (SCCM)	F_{H_2} (SCCM)	F_{Ar} (SCCM)	F_{H_2O} (SCCM)
39.47	17.7	6.47	119.5

Subsequently, this wet gas mixture is directed into the tubular reforming reactor which includes a washcoated catalyst and where heat is provided by the DC power source. After the reforming reactions take place inside the reactor, the outlet gases are cooled down to room temperature in order to safeguard the gas chromatography (GC) apparatus. During this cooling phase, the steam is condensed, and the resulting condensate is collected in the steam condenser. This condensed gas mixture is subsequently analyzed using the GC system and then it is released as vent gas. More details of the experimental setup can be found in Çıtmacı et al. (2024).

Remark 1. Before the experiment, the expected amount of steam is calculated by defining a steam-to-carbon ratio, calculated using the Antoine equation, which yields partial pressure as a function of temperature. These equations were checked with respect to steam box temperature signals (sensed by a thermocouple) to have a good approximation of the initial steam flowrate.

Remark 2. In an industrial hydrogen production process, outlet gases of SMR reactors will typically go through shift reactors to convert the remaining CO to CO_2 to produce more H_2, and then, the gases pass through a pressure swing absorption (PSA) separation process to separate pure hydrogen from the shift reactor outlet gas mixture (Molburg and Doctor, 2003).

3.2. Automation of the experimental system

This section discusses the automatic devices and data collection platforms used to operate the experimental, electrified SMR process. Specifically, devices involve sensors and actuators, which are commonly used in modern industries. In the SMR experiment, several sensors were utilized to measure in real-time key process variables, such as the reactor temperature, the system pressure, and the H_2

production rate. GC is the sensor used to measure the composition of each gas in the reactor outlet. By using Argon as the tracer, the flowrate of each gas entering the GC is also measured. Thermocouples are used to measure the temperature. In the experiment, temperatures at both ends of the reactor and the steam box are measured. Actuators were used to manipulate the process inputs that have to be manipulated to implement the control actions. In this process, the current is the manipulated input, and it can be manipulated by the DC power source, making the DC power source the control input actuator. The flowrate of each species and the pressure of the whole system can be also manipulated by the flow-meters and the back pressure regulator as actuators, respectively. These devices are set to ensure those parameters were constant during the experiment.

All the actuator and sensor devices are digitalized by the Laboratory Virtual Instrument Engineering Workbench (LabVIEW) interface. The LabVIEW interface is further connected to the Smart Manufacturing Institute's (CESMII) Innovation Platform (SMIP). The platform receives the information from the sensors by the query language GraphQL, to calculate the required values to be sent to the actuator, and to finally manipulate the actuator to implement the updated values in the experimental reactor. By using the above elements, a real-time automatic feedback control can be implemented on the process.

Remark 3. The flowrate measured by the GC is shown in the unit of Standard Cubic Centimeters per Minute ($SCCM$). The transformation of this unit to the SI unit is given by the following equation:

$$1\frac{\text{mol}}{\text{s}} = \frac{10^{-3}\frac{\text{L}}{\text{cm}^3}}{22.4\frac{\text{L}}{\text{mol}} \cdot 60\frac{\text{s}}{\text{min}}} \cdot \frac{\text{cm}^3}{\text{min}} = 7.44 \cdot 10^{-7} SCCM \tag{7}$$

The $22.4\frac{\text{L}}{\text{mol}}$ molar volume is chosen since the SCCM is based on the Standard Temperature and Pressure (STP) condition.

4. Model development and validation

In this section, a first-principle model is initially developed for the experimental setup using a lumped-parameter approach (Çıtmacı et al., 2024) to capture the dynamic behavior of this specific SMR system. For this model, the initial parameters are obtained from relevant literature or derived from experimental observations. Additionally, the reliability of the model is tested by comparing its results with experimental data. This first-principle model further serves as the model for subsequent implementation in a real-time model predictive control strategy. It is important to point put that employing a full data-based approach requires very large data sets that are not available for the present experimental system and this is why we employ a hybrid modeling approach combining first-principles modeling with well-known reaction kinetics with experimental data.

4.1. First-principles model development

For the modeling of the experimental reactor, a continuous stirred-tank reactor (CSTR) approach with a spatially uniform concentration distribution of each species is assumed. These assumptions are based on the following factors. Firstly, the reaction dynamics are very fast compared to the residence time, so the reaction is mainly occurring in the beginning part of the tubular reactor. Hence, the majority of the reactor (after the beginning part where the reforming reactions occur) has a uniform concentration distribution and can be approximated as a CSTR. Secondly, the lumped parameter model influenced by the CSTR approach is easy to build and needs a much lower computational cost to conduct inferences with. Due to these considerations, the mass balance equations accounting for temperature-based variables (e.g., volumetric flowrate) are derived similarly as in Çıtmacı et al. (2024).

The first-principle model can be constructed based on the mole balance of each species for the lumped-parameter case, considering two reactions (Eq. (1)). However, this ordinary differential equation system can only be utilized when the volumetric flowrate (q) and kinetic rate expressions (r_1 and r_2) are fully defined, as these quantities are time-varying as well. The mole balances of each species are as follows:

$$\frac{dC_{CH_4}}{dt} = \frac{1}{V_R}\left(F_{CH_4,0} - r_1 W - q C_{CH_4}\right) \tag{8a}$$

$$\frac{dC_{H_2O}}{dt} = \frac{1}{V_R}\left(F_{H_2O,0} - (r_1 + r_2) W - q C_{H_2O}\right) \tag{8b}$$

$$\frac{dC_{CO}}{dt} = \frac{1}{V_R}\left(F_{CO,0} + (r_1 - r_2) W - q C_{CO}\right) \tag{8c}$$

$$\frac{dC_{H_2}}{dt} = \frac{1}{V_R}\left(F_{H_2,0} + (3r_1 + r_2) W - q C_{H_2}\right) \tag{8d}$$

$$\frac{dC_{CO_2}}{dt} = \frac{1}{V_R}\left(F_{CO_2,0} + r_2 W - q C_{CO_2}\right) \tag{8e}$$

$$\frac{dC_{Ar}}{dt} = \frac{1}{V_R}\left(F_{Ar,0} - q C_{Ar}\right) \tag{8f}$$

where $F_{i,0}$ is the inlet molar flowrate of species i. C_i is the concentration of species i, q is the volumetric flowrate.

The volumetric flowrate, q, is expressed using the ideal gas law (Eq. (9)) and the mole balance (Eq. (8)) as shown in Eq. (10). A more detailed derivation is shown in Çıtmacı et al. (2024).

$$C_T = C_{CH_4} + C_{H_2O} + C_{CO} + C_{H_2} + C_{CO_2} + C_{Ar} = \frac{P}{RT} \tag{9}$$

$$q = \frac{F_{T0} + 2r_1 W}{\frac{P}{RT}} + \frac{V_R}{T}\frac{dT}{dt} \tag{10}$$

For the kinetic rate equations of an SMR system, numerous works on modeling it have been established to study the dynamic behavior. In this paper, the rate expressions in Eq. (11) are obtained from Xu and Froment (1989). First, Xu and Froment (1989) employed a Nickel-based catalyst to initiate the reaction, which is also utilized in our experiments. Second, Xu and Froment (1989) did not incorporate mass transfer or fluid dynamic equations; instead, they concentrated solely on the two fundamental reactions. Thirdly, several physical parameters, such as reactor volume and catalyst weight, closely resemble those of our experimental setup. Therefore, it is reasonable to utilize the reaction rates from Xu and Froment (1989) as follows:

$$r_{1,SMR} = \frac{k_1}{P_{H_2}^{2.5}}\frac{P_{CH_4} P_{H_2O} - \frac{P_{H_2}^3 P_{CO}}{K_1}}{(DEN)^2} \tag{11a}$$

$$r_{2,WGS} = \frac{k_2}{P_{H_2}}\frac{P_{CO} P_{H_2O} - \frac{P_{H_2} P_{CO_2}}{K_2}}{(DEN)^2} \tag{11b}$$

$$DEN = 1 + K_{CO} P_{CO} + K_{H_2} P_{H_2} + K_{CH_4} P_{CH_4} + K_{H_2O}\frac{P_{H_2O}}{P_{H_2}} \tag{11c}$$

$$k_j = A_j \exp\left(-\frac{E_j}{RT}\right), \quad j = 1, 2 \tag{11d}$$

$$K_i = A_i \exp\left(-\frac{\Delta H_i}{RT}\right), \quad i = CH_4, H_2O, CO, H_2 \tag{11e}$$

The purpose of the first-principle model is to establish the relationship between the input variable and the state variables. Motivated by the dynamic behavior observed in the mole balance equations of the reactor, the concentration of the six gas species is selected as the state variables. However, in this experiment, direct detection of the concentration is not feasible. As a result, the concentration must be converted into measurable physical information. In this experiment, the H_2 production rate (F_{H_2}) and the reactor temperature (T) are the only detectable physical information, measured using the GC and the thermocouple, respectively. Hence, the H_2 concentration should be converted to the H_2 production rate using Eq. (12) for use in the model.

$$F_{H_2} = q C_{H_2} \tag{12}$$

The manipulated input variable represents the physical parameter that we can manipulate, which is the current (I) in our case. By adjusting the current, the heat supply to the process is modified, thereby influencing the temperature inside the reactor. The temperature appears in the mole balance equations, implying state variables will be influenced by the temperature. The quantitative impact of temperature on the dynamics has been shown in Eq. (8), so the only required quantitative relationship remaining to capture is that between the current and the temperature. This relationship can be built based on an energy balance as follows:

$$\frac{dT}{dt} = \frac{I^2 \bar{R} + \sum_i \dot{m}_{p_i} C_{p_i}(T_0 - T) - W r_{SMR} \Delta H_{SMR}(T) - W r_{WGS} \Delta H_{WGS}(T) + U A(T_s - T)}{\sum_i \rho_i C_{p_i} V_R} \tag{13}$$

which is the modified version of the energy balance shown in Fogler (2020) and the current is introduced by the heat supply term representing power dissipation ($I^2 \bar{R}$) as per Joule's law.

Remark 4. The perfect mixing assumption leading to the development of the lumped parameter model implies also that the temperature does not vary along the length of the reactor. However, due to the endothermic and exothermic reactions of the SMR system, the temperature varies along the reactor in the actual experiment. Hence, selecting an appropriate temperature to represent the overall reactor temperature is essential in the model. For the simulation, the temperature is chosen to be the weighted average of temperatures at both ends as follows:

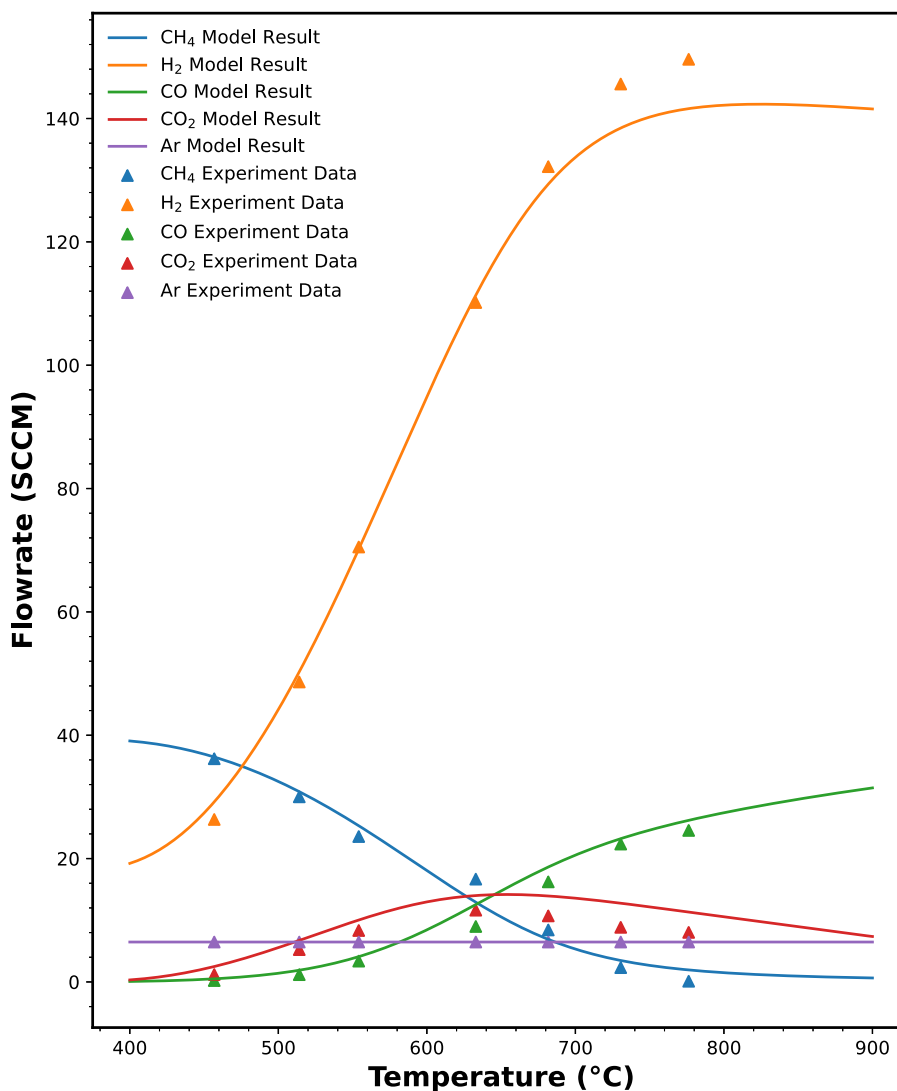$$T_m = T_{ave} = 0.6 T_{top} + 0.4 T_{bottom} \tag{14}$$

Fig. 2. Steady-state flowrate of different gas species at different temperatures. The triangle data points are averages of steady-state experimental data points at each temperature (used in the model development), and the solid lines represent the steady-state model solution at various temperatures.

where T_{ave}, T_{top} and T_{bottom} represent the weighted average temperature, the temperature at the inlet section of the reactor (34.5 cm from the reactor end), and the temperature at the outlet section of the reactor (13.5 cm from the reactor end) respectively.

Remark 5. For the energy balance shown in Eq. (13), the resistance term ($\bar{R}$) was determined by the linear regression fitting of the potential (E) and the current (I) according to Ohm's Law:

$$E = I\bar{R} \tag{15}$$

4.2. First-principles model parameter estimation and validation

In Section 4.1, the relationship between the control input (current, I) and control output (H_2 production rate, F_{H_2}) has been presented. In this section, the parameters appearing in these equations will be estimated and the resulting model will be validated.

Specifically, these parameters can be categorized into two groups: kinetic rate parameters and heat transfer parameters. For the parameters in the kinetic rate equations, two pre-exponential factors (A_j) and two activation energies (E_j) need to be determined. Since the experiment has similar conditions to Xu and Froment (1989), the same

parameter values are assumed initially. For the heat transfer parameter, the parameters that have to be determined are the heat transfer coefficient (U) and the surface area of the reactor (A). Since these two parameters are both unknown, and they only appear in product form, they can be regarded as a single parameter (UA) that should be determined by fitting the experimental data. Specifically, the least squares method is employed to determine the value of UA. The goal is to minimize the discrepancy between the experimental data and the simulation results by adjusting the unknown parameters. In this case, UA is the parameter to be fitted to the temperature data, since the UA only occurs in the energy balance shown in Eq. (13). This is achieved by varying UA until the difference between the experimental temperature data and model estimates of the temperature for that value of UA is minimized. This least-squares formulation can be expressed by the following minimization problem:

$$\mathcal{J} = \min_{UA} \; L(I_i, UA) \tag{16a}$$

$$\text{s.t.} \quad X = \{X \,|\, F(X, I_i, UA) = 0\} \tag{16b}$$

$$T_{fp} = x_7 \tag{16c}$$

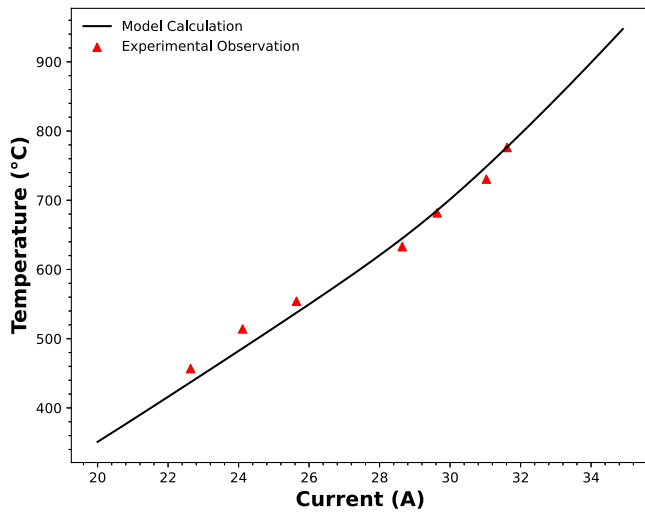$$L(I_i, UA) = \sum_{i=1}^{N} (T_{fp} - T_m(I_i))^2 \tag{16d}$$

Fig. 3. Reactor temperature variation with respect to current at steady state.

where UA is the parameter required to be determined, I_i is the current value for the ith data, $F(\cdot) = 0$ is the first principle model with steady state condition, X is the state values estimated by the first principle model for $X = x_1, x_2, \ldots, x_7$, N is the total number of data points, T_{fp} is the reactor temperature estimation from the first principle model, and $T_m(I_i)$ is the experimentally measured reactor temperature corresponding to the specific current (I_i).

Multiple steady-state experiments were conducted to test if the first principle model is reliable, and their results were further used to compare to the model outputs. First, the reliability of the kinetic parameters is tested by the steady-state flowrate of 5 species at different temperatures. In the experiment, the steady-state flowrates at 6 different temperatures within 400–900 °C range were measured via GC. In the simulation, all flowrates within this temperature range are calculated. The comparison plot is shown in Fig. 2. From this comparison plot, the experimental data shows close correspondence to the predictions of the model, indicating the parameters from Xu and Froment (1989) are acceptable in our case.

To find the heat transfer parameters in the energy balance (UA in Eq. (13)), temperatures at the steady state and their corresponding currents were used from the experimental data. For each current value, the temperature measurements can be calculated combining Eqs. (8) and (13). After solving the minimization problem in Eq. (16), the UA term was determined to be 0.114 J (s K)$^{-1}$. By applying this value, the comparison of the experimental data and the simulation results from the model was compared in Fig. 3. The data presented herein demonstrates that the model effectively forecasts the temperature readings obtained from the thermocouple.

Remark 6. SMR process suffers from coke formation side reactions at higher temperatures (Zhang et al., 2021). This might affect the model predictions, since the modeling strategy described in Section 4.1 does not account for coke formation. There are multiple probable coke formation mechanisms that might be happening in the reactor (Ginsburg et al., 2005; Ashik et al., 2017). However, carbon formation is difficult to qualitatively model. The sensor feedback is expected to influence the model predictions for possible carbon formation on the catalyst.

Remark 7. The value of UA directly impacts the heat loss of the reactor. During the experiment, the addition of insulation material resulted in a significantly reduced heat loss, suggesting a much smaller value for UA.

5. Feedback control

In this section, a feedback control strategy is developed to regulate the H_2 production rate in the SMR system by adjusting the current. Specifically, a model predictive controller is formulated to achieve this objective, incorporating the extended Luenberger observer method for complete state estimation. The performance of this ELO estimation-based MPC is demonstrated through a comparison with PI control, and its robustness is further evaluated by introducing a disturbance.

5.1. Extended luenberger observer equations development

To implement the MPC, all state variables should be known to be utilized as the initial values to predict the target output in the receding horizons. However, in this specific system, only the reactor temperature from the thermocouple and the H_2 production rate from the GC are directly measurable. Therefore, to address this limitation, an Extended Luenberger Observer scheme is introduced to estimate all state variables, including concentrations for all species and reactor temperature. The ELO estimation employs a system of ODEs that integrates both the first-principles model and the error between measurement and model. Consequently, the ELO dynamic equations are formulated as the modified mole balance equations from Eq. (8) and the modified energy balance equation from Eq. (13) as follows:

$$\frac{d\hat{C}_{CH_4}(t)}{dt} = \frac{1}{V_R}\left(F_{CH_4,0} - r_1(t)W - \hat{q}(t)\hat{C}_{CH_4}(t)\right) + K_{T,1}\left(T_M - T(t)\right) + K_{H_2,1}\left(F_{H_2M} - \hat{F}_{H_2}(t)\right) \quad (17a)$$

$$\frac{d\hat{C}_{H_2O}(t)}{dt} = \frac{1}{V_R}\left(F_{H_2O,0} - (r_1(t)+r_2(t))W - \hat{q}(t)\hat{C}_{H_2O}(t)\right) + K_{T,2}\left(T_M - T(t)\right) + K_{H_2,2}\left(F_{H_2M} - \hat{F}_{H_2}(t)\right) \quad (17b)$$

$$\frac{d\hat{C}_{CO}(t)}{dt} = \frac{1}{V_R}\left(F_{CO,0} + (r_1(t)-r_2(t))W - \hat{q}(t)\hat{C}_{CO}(t)\right) + K_{T,3}\left(T_M - T(t)\right) + K_{H_2,3}\left(F_{H_2M} - \hat{F}_{H_2}(t)\right) \quad (17c)$$

$$\frac{d\hat{C}_{H_2}(t)}{dt} = \frac{1}{V_R}\left(F_{H_2,0} + (3r_1(t)+r_2(t))W - \hat{q}(t)\hat{C}_{H_2}(t)\right) + K_{T,4}\left(T_M - T(t)\right) + K_{H_2,4}\left(F_{H_2M} - \hat{F}_{H_2}(t)\right) \quad (17d)$$

$$\frac{d\hat{C}_{CO_2}(t)}{dt} = \frac{1}{V_R}\left(F_{CO_2,0} + r_2(t)W - \hat{q}(t)\hat{C}_{CO_2}(t)\right) + K_{T,5}\left(T_M - T(t)\right) + K_{H_2,5}\left(F_{H_2M} - \hat{F}_{H_2}(t)\right) \quad (17e)$$

$$\frac{d\hat{C}_{Ar}(t)}{dt} = \frac{1}{V_R}\left(F_{Ar,0} - \hat{q}(t)\hat{C}_{Ar}(t)\right) + K_{T,6}\left(T_M - T(t)\right) + K_{H_2,6}\left(F_{H_2M} - \hat{F}_{H_2}(t)\right) \quad (17f)$$

where $\hat{C}_i$ is the estimated concentration for $i = CH_4, H_2O, CO, H_2 CO_2$. $K_{T,i}$ and $K_{H_2,i}$ are the observer gains for the temperature error and the H_2 production rate error, respectively, for $i = 1,2,3,4,5,6$, and T_M and F_{H_2M} are real-time measurements of the reactor temperature and H_2 production rate, respectively. The equation for temperature estimation is as follows:

$$\frac{d\hat{T}(t)}{dt} = \frac{I^2\bar{R} + \sum_i \dot{m}_{p_i}C_{p_i}(T_0 - \hat{T}) - Wr_{SMR}\Delta H_{SMR}(\hat{T}) - Wr_{WGS}\Delta H_{WGS}(\hat{T}) + UA(T_s - \hat{T})}{\sum_i \rho_i C_{p_i} V_R} + K_{T,7}\left(T_M - \hat{T}(t)\right) \quad (18)$$

where $\hat{T}$ is the estimated reactor temperature, and $K_{T,7}$ is the observer gain. In Eq. (17), the error term of the flowrate is based on the conversion of the state variables from molar flowrate of each species to sccm. Therefore, the following relationship should be used to relate the concentration and molar flow rate of hydrogen when solving the

dynamic ODE system:

$$\hat{F}_{\mathrm{H}_2} = \hat{q}\hat{C}_{\mathrm{H}_2} \tag{19}$$

The expression for the volumetric flowrate ($\hat{q}$) in the ELO estimation should be adjusted accordingly, as $\hat{q}$ is derived from equations involving the mole balance and the energy balance equations and these equations undergo modification when the ELO estimation is applied. Except for the mole balance and the energy balance, the $\hat{q}$ is also derived based on the ideal gas law,

$$\hat{C}_T = \hat{C}_{\mathrm{CH}_4} + \hat{C}_{\mathrm{H}_2\mathrm{O}} + \hat{C}_{\mathrm{CO}} + \hat{C}_{\mathrm{H}_2} + \hat{C}_{\mathrm{CO}_2} + \hat{C}_{\mathrm{Ar}} = \frac{P}{R\hat{T}} \tag{20}$$

where $\hat{C}_T$ is the total gas concentration in the reactor. From this equation, the derivative of the total concentration can be calculated by Eq. (21a), while the derivative of the total concentration can also be calculated by Eq. (21b) from the summation of the mole balance of each species.

$$\frac{\mathrm{d}\hat{C}_T}{\mathrm{d}t} = -\frac{1}{\hat{T}^2} \cdot \frac{P}{R} \cdot \frac{\mathrm{d}\hat{T}}{\mathrm{d}t} \tag{21a}$$

$$\frac{\mathrm{d}\hat{C}_T}{\mathrm{d}t} = \frac{1}{V_R} \cdot \left(F_{T,0} + 2r_1 W - \hat{q}\hat{C}_T \right) + \left(\sum_{i=1}^{6} K_{T,i} \right) \left(T_M - \hat{T}(t) \right)$$

$$+ \left(\sum_{i=1}^{6} K_{\mathrm{H}_2,i} \right) \left(F_{\mathrm{H}_2 M} - \hat{F}_{\mathrm{H}_2}(t) \right) \tag{21b}$$

Combining the two subequations in Eq. (21), a new expression of volumetric flowrate can be developed,

$$\hat{q} = \frac{F_{T0} + 2r_1 W + V_R \left(\left(\sum_{i=1}^{6} K_{T,i} \right) \left(T_M - \hat{T}(t) \right) + \left(\sum_{i=1}^{6} K_{\mathrm{H}_2,i} \right) F_{\mathrm{H}_2 M} \right)}{\frac{P}{R\hat{T}} + \left(\sum_{i=1}^{6} K_{\mathrm{H}_2,i} \right) C_{\mathrm{H}_2}}$$

$$+ \frac{V_R}{\hat{T}} \frac{\mathrm{d}\hat{T}}{\mathrm{d}t} \tag{22}$$

where $\frac{\mathrm{d}\hat{T}}{\mathrm{d}t}$ represents the modified energy balance equation with the error term (Eq. (18)).

Remark 8. When simulating control based on experimental conditions, it is imperative to consider the actual measurement sampling time and sensor time delay. In our case, the thermocouple measurement has a sampling time of 1 s ($\Delta t_T = 1$ s). However, due to the computational intensity of the MPC, calculating a control input can take more than one second and cause delays. Therefore, a 5-second thermocouple sampling time ($\hat{\Delta}t_T = 5$ s) is chosen, and control actions are adjusted accordingly, such that it is computed every 5 s. For GC measurements, analysis takes 15 min, followed by a 3-minute cooldown. Thus, the GC data measurement has an 18-minute sampling time ($\Delta t_{GC} = 18$ min) and a 15-minute time delay ($\tau_{GC,delay} = 15$ min). During each sampling time, the measurements (T_M and $F_{\mathrm{H}_2 M}$) remain constant, while the corresponding ELO estimations (T and F_{H_2}) vary over time. Consequently, the error term in the ODEs also evolves dynamically.

Remark 9. For Eq. (18), the observer error term pertains specifically to temperature errors. This is because temperature measurements from the thermocouple are frequent and accurate. Therefore, adjusting temperature values solely based on the temperature measurements suffices when employing a large observer gain in the energy balance equation. It is also important to point out that we did test the robustness of the observer gains determined above and used in our simulations with respect to measurement noise and found them to be suitable; however, in the experimental implementation of the developed controller, we expect that further fine-tuning may be needed.

Remark 10. In Section 2, the criteria for selecting appropriate observer gains of the error term ($K_{T,i}$ and $K_{\mathrm{H}_2,i}$ for $i = 1, 2, 3, 4, 5, 6$) were discussed. Specifically, to ensure local exponential stability of the observer error equation, the linearized observer error system around the

steady state point must satisfy the condition where the real parts of all eigenvalues of the matrix $A - KH$ in Eq. (5) are strictly negative. Based on this constraint, the observer gain is further tuned through numerous simulations across different initial conditions and various disturbance cases. Specifically, $K_{T,i}$ is tuned to achieve a good estimation error convergence for all state values. In particular, since the reactor temperature is accurately measured in real-time, a larger observer gain ($K_{T,7}$) is used to multiply the temperature error term in the observer equations. Tuning $K_{\mathrm{H}_2,4}$ (observer gain for H_2) presents challenges due to the infrequency and delay present in the GC measurements. If $K_{\mathrm{H}_2,4}$ is too large, the estimated H_2 production rate lacks accuracy in dynamic regions compared to the real production rate, as the observer error term relies on measurements that involve significant time delay. Conversely, if $K_{\mathrm{H}_2,4}$ is too small, the ELO estimation resembles the pure model estimates and exhibits an offset between the estimated and real H_2 production rates in both dynamic and steady-state regions. In this context, a relatively large observer gain for H_2 is chosen because it provides a good estimation for the final steady state. This choice is based on the fact that in the final steady state, the real H_2 production rate remains constant, resulting in accurate measurements despite time delays and sampling intervals. For other observer gain values ($K_{\mathrm{H}_2,i}$ for $i = 1, 2, 3, 5, 6$), they are tuned to achieve a good estimation for the other flowrates. Finally, the local exponential stability of the closed-loop system is ensured provided the feedback controller (whether PI or MPC) achieves local exponential stability under full state feedback and the state estimator error dynamics are also locally exponentially stable.

5.2. Closed-loop results under PI control and MPC

To develop a robust controller, we construct and compare both a PI control scheme and an MPC scheme. Subsequently, the disturbance rejection capability is assessed in the subsequent section to demonstrate robustness. For the control scenario in our case, the controlled variable is the H_2 production rate, and the control input is the current. Initially, the system is at a steady-state at an initial temperature of 514 °C and an initial hydrogen production rate of 51.4 SCCM for 10 min. After that, the set-point of the hydrogen production rate changed to 120 SCCM. Notably, the current value is constrained to be 40 A or lower, because a high current will lead to a large reactor temperature, which may damage the catalyst. Specifically, the PI controller can be described by the following set of equations:

$$u = K_c \cdot \left[\left(y_{sp} - y \right) + \frac{1}{\tau_I} \int_0^t \left(y_{sp} - y \right) \mathrm{d}\tau \right] \tag{23a}$$

$$u = I - I_s \tag{23b}$$

$$y_{sp} = F_{\mathrm{H}_2, sp} - F_{\mathrm{H}_2,s} \tag{23c}$$

$$y = F_{\mathrm{H}_2} - F_{\mathrm{H}_2,s} \tag{23d}$$

$$0 \text{ A} \leq I \leq 40 \text{ A} \tag{23e}$$

where u is the control action in deviation form, K_c and τ_I are the PI controller tuning parameters, y is the measured output, and y_{sp} is the set-point.

The closed-loop simulation results under PI control are shown in Fig. 4. The left two figures show the current change from the PI controller and the corresponding impact on the temperature. The right two figures show the H_2 production rate received by the PI controller and the simulated ground truth. At the beginning, the current is 25 A and the H_2 production rate is 51.4 SCCM and the system is at the steady state for 10 min, so the current and the H_2 production rate were constant. At $t = 10$ min, the control started, so the current is changed by the PI controller, resulting in the variation of H_2 production rate to close to the set-point. During closed-loop operation under PI control, the sampling time is one second, while the measurement of H_2 production rate is sent to the controller every 18 min and involves a 15 min delay in order to emulate realistic GC measurement system sampling
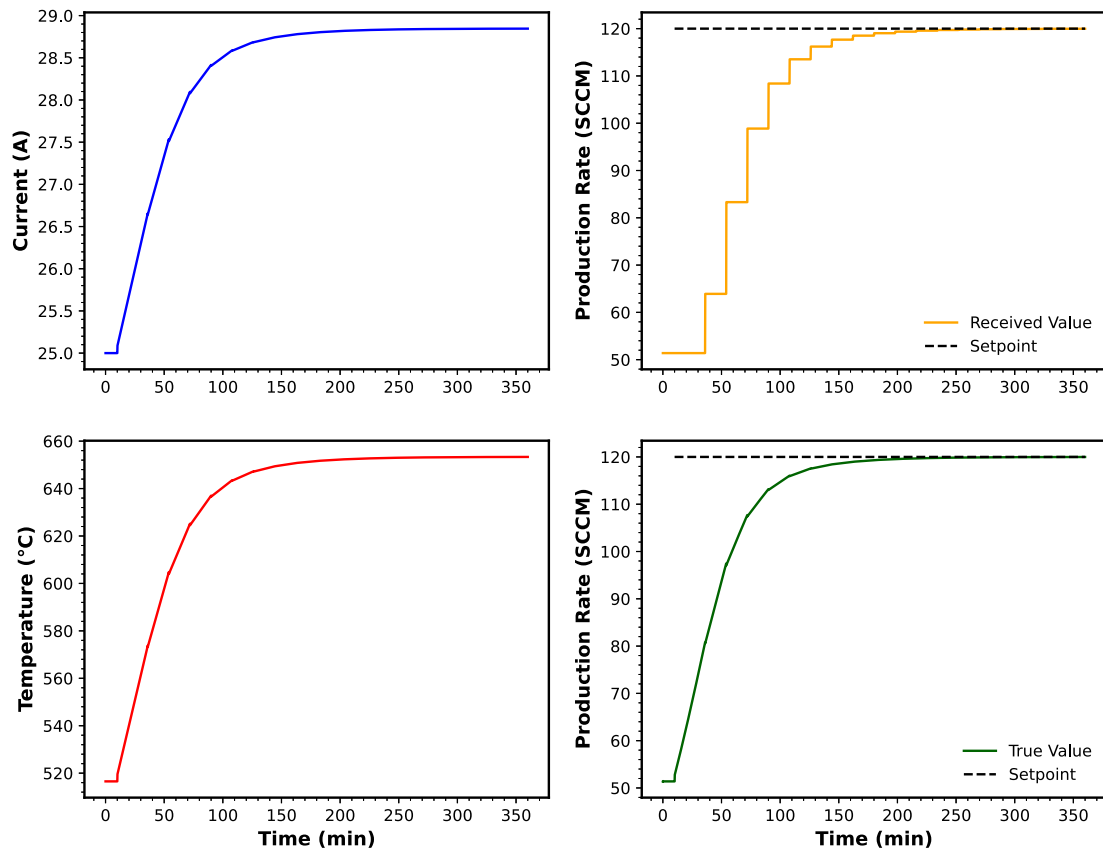
Fig. 4. Closed-loop H_2 production rate and control action under PI control for nominal case.
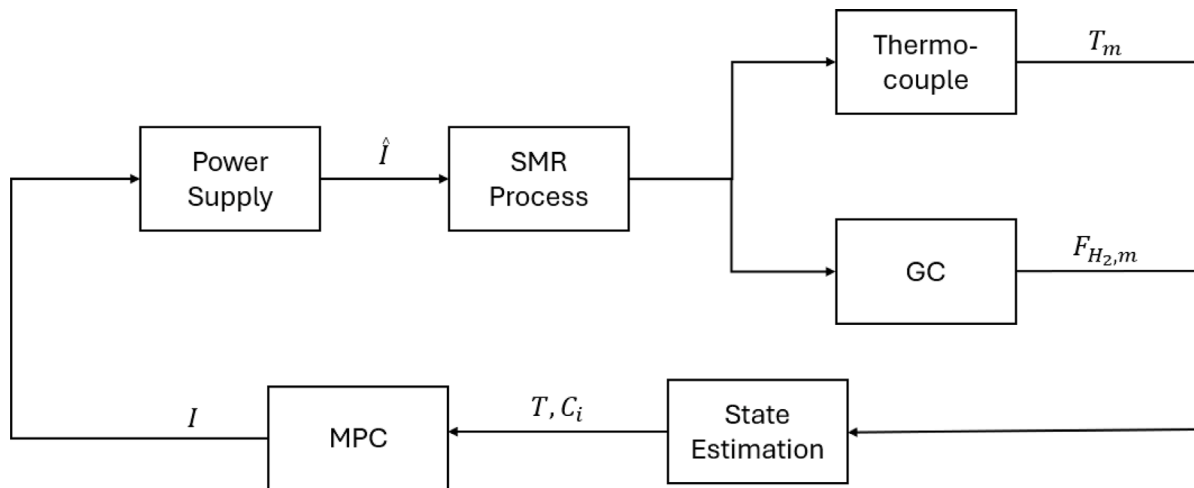

Fig. 5. Closed-loop system structure under estimation-based MPC for the SMR process.

and delay times. Therefore, the received H_2 production rate is assumed to be constant within each sampling time, which is shown in the top-right figure in Fig. 4. Even though the proportional error term remains constant, the integral error term varies due to the error accumulation over time. Consequently, the control input changed correspondingly to drive the H_2 production rate to the set-point. Around $t = 177$ min, the H_2 production rate reaches at the set-point (within 1% error) with the corresponding current at $I = 28.8$ A.

The closed-loop system structure under MPC is shown in Fig. 5. Sensor measurements (reactor temperature T_m and H_2 production rate F_{H_2}) are first used for the state estimation by the ELO before the model predictive controller. The corresponding ELO estimation equations have

been shown in Section 5.1. The MPC calculates the required control input (I) and sends it to the power supply. The power supply gave the SMR system the applied current ($\hat{I}$), so the reactor temperature and the H_2 production rate change accordingly. These 2 measurable parameters were captured by the sensors (thermocouple and GC) and then used for the state estimation. The MPC algorithm takes the following specific form:

$$\mathcal{J} = \min_{I} \int_{t_k}^{t_{k+N_h}} L(\bar{x}(t), I(t)) \, \mathrm{d}t \tag{24a}$$

$$\text{s.t. } \dot{\bar{x}}(t) = ODE(\bar{x}(t), I(t)), \ \bar{x}(t_k) = \hat{x}(t_k) \tag{24b}$$
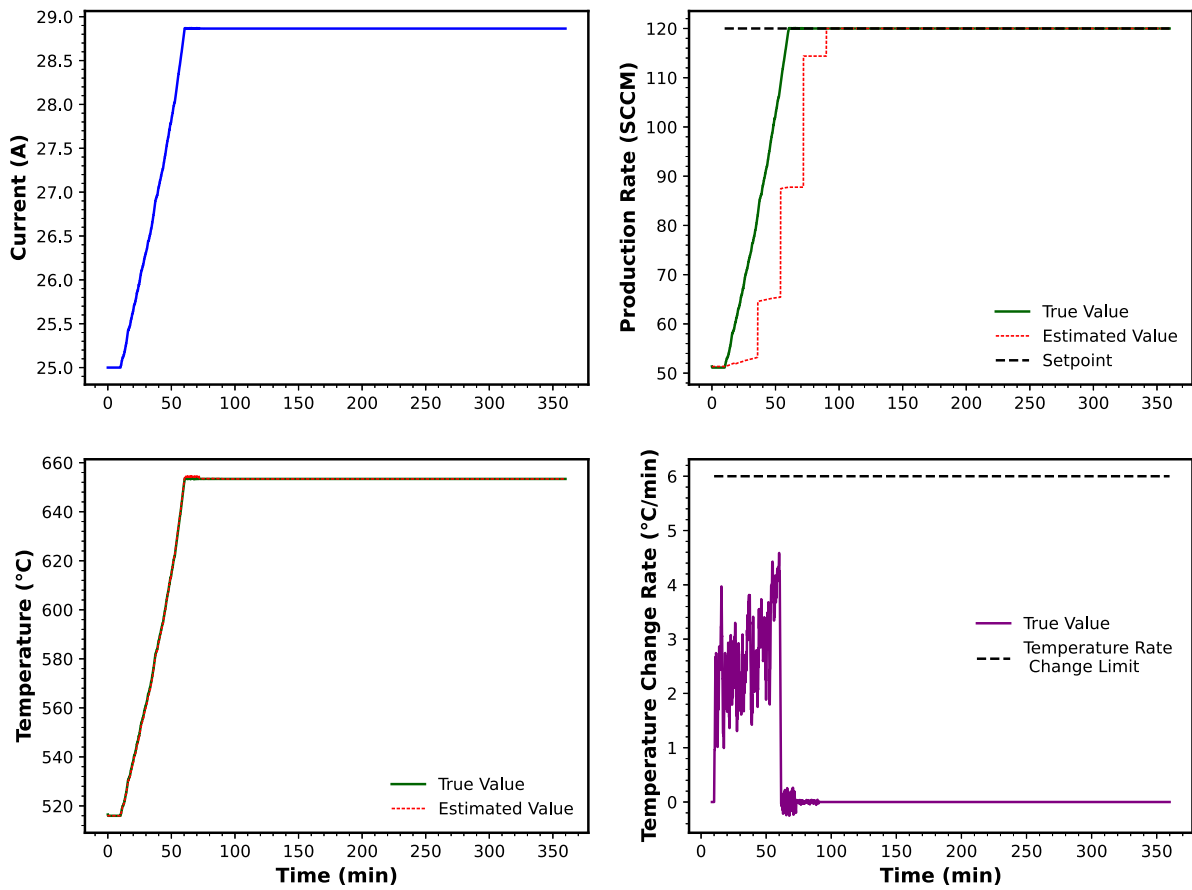
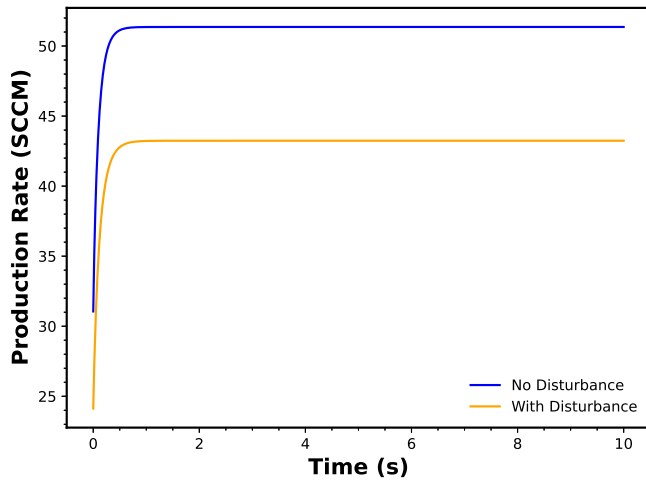**Fig. 6.** Closed-loop H_2 production rate and control action under MPC for nominal case.

Fig. 7. Comparison of H_2 production rate for disturbance and no disturbance cases under open-loop conditions with the temperature set at 514 °C.

$$\bar{F}_{H_2}(t) = h(\bar{x}(t)) \tag{24c}$$

$$L(\bar{x}(t), I(t)) = A(\bar{F}_{H_2}(t) - F_{H_2,sp})^2 + B(I(t) - I_{sp})^2 \tag{24d}$$

$$t \in [t_k, t_{k+N_h}) \tag{24e}$$

$$|I(t_k) - I(t_{k-1})| \le \Delta I_c \tag{24f}$$

$$0 \text{ A} < I < 40 \text{ A} \tag{24g}$$

In particular, the minimization problem is set as in Eq. (24). The state variables (x) are the reactor temperature and the concentration of each species in the reactor. The manipulated input is the current (I). $F_{H_2,sp}$ and I_{sp} are the set-point of the H_2 production rate and the expected current at the set-point, respectively. For the state prediction in the receding horizons, Eq. (24b) comprises the ODEs of the mole balance equations, Eq. (8), and the energy balance, Eq. (13). The function $h(\cdot)$ in Eq. (24c) is employed to map the state value to the sensor measurement. Specifically, it transforms the concentration prediction to the H_2 production rate. The cost function, Eq. (24d), was the combination of the difference of the H_2 production rate from its set-point and the difference between the current and the corresponding set-point current. A and B are the coefficients for each term, respectively. When tuning A and B, the first term in the cost function should be larger than the second term. This ensures that solving the minimization problem primarily emphasizes the disparity in H_2 production rates rather than the current. Eq. (24g) is the range bound for current that also appears in the PI control algorithm; however, the MPC also defines constraints on the rate of change of the control input itself as per Eq. (24f), which is not utilized in PI. This constraint is crucial since any sudden and extreme change in the reactor temperature will damage the catalyst, implying the change of current should also be limited. The upper limit of the rate of change of temperature is determined based on the work conducted by Zhao et al. (2020), as they utilized the same type of catalyst in their experiment. In their study, the rate of change of temperature was set to 10 °C/min. However, Zhao et al. (2020) implemented the SMR experiment under low-temperature conditions (550 °C). At higher temperatures, coke formation becomes more prevalent, suggesting the need for a more conservative temperature change rate
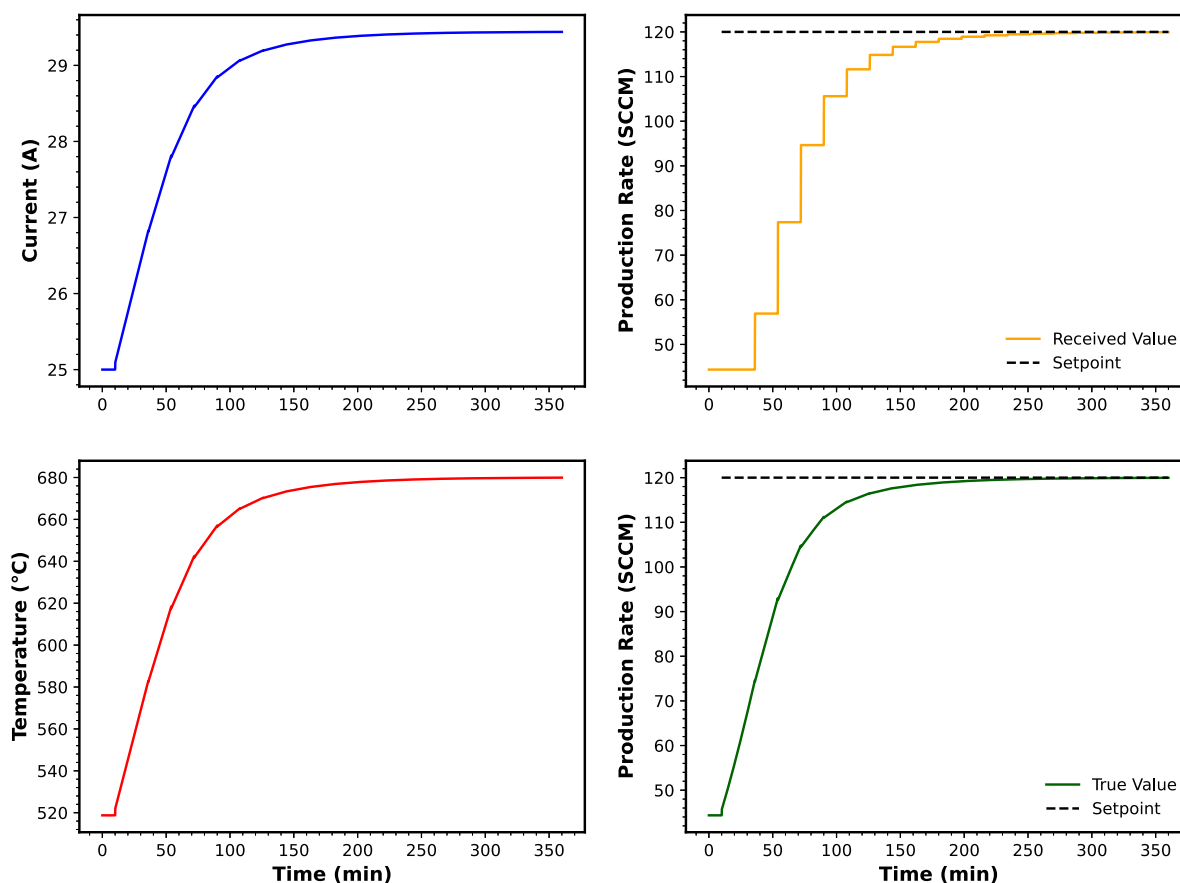
Fig. 8. Closed-loop H_2 production rate and control action under PI control in the presence of process variability.

constraint. Therefore, based on this consideration and past experimental results, a limit of 6 °C/min is chosen as the upper threshold for the temperature change rate. From the quantitative relationship of the temperature and the current (Fig. 3), the corresponding limit for the current change from one sampling time to the next should be 0.013 A. From a safety perspective, the limit on the current change, ΔI_c in Eq. (24f), is set to be 0.01 A.

To solve this nonlinear, constrained minimization problem, the Sequential Quadratic Programming (SQP) method is applied. The SQP method is derived by solving the Kuhn–Tucker conditions of a nonlinear, constrained optimization problem using the Newton method. It is a direct extension of the Newton–Raphson method, benefiting from its Newton-like properties, which enable it to converge in relatively few iterations. Therefore, SQP is renowned for its speed in solving minimization problems compared to other approaches and has been widely utilized in practical applications due to its efficiency (Boggs and Tolle, 1995). Due to the time-efficient property, utilization of the SQP method to solve the minimization problem facilitates the implementation of MPC in real-time.

The results of the MPC are illustrated in Fig. 6. At both the initial and final steady-states, the current and the H_2 production rate were the same as in the case of PI control. However, the MPC is significantly faster than PI in terms of driving the H_2 production rate to the set-point. For the MPC case, the time required to reach around the set-point with a 1% error is 52 min, while for the PI case, it is 167 min. The bottom-left plot in Fig. 6 shows the reactor temperature as a function of time under closed-loop MPC. The bottom-right plot in Fig. 6 shows the change in temperature between the current temperature and the value from 1 min before, indicating that the largest temperature change rate is lower than 6 °C/min, which is favorable for the catalyst. Regarding

computational time, the MPC simulation requires only 102 min of real time to simulate a total time of 360 min using the lumped-parameter-based first-principle model in MPC, making implementation in real-time experiments feasible.

Remark 11. The set-point is selected to reflect a substantial deviation from the initial H_2 production rate, aiming to evaluate the controller's efficacy in accommodating significant changes. It is crucial for this set-point to be attainable within the system's H_2 production capabilities. Hence, the theoretical range of the H_2 production rate is computed to verify if the selected set-point falls within this range.

Remark 12. For the PI control, the received H_2 production rate is depicted as it changes over time during the controlled process in the top-right plot of Fig. 4. Several important considerations should be noted. Firstly, the received H_2 production rate remains constant during each sampling interval (18 min). Secondly, due to a 15-minute delay in measurement from the GC, the H_2 production rate reflects conditions from 15 min before. Consequently, the control action is determined based on the larger difference between the current H_2 production rate and the set-point since the H_2 production rate was much closer to the set-point at the moment when a control action should be made compared to the H_2 production rate that the PI received (i.e. the observed difference is larger than the true difference). Additionally, to protect the catalyst, the temperature change rate should not be aggressive. However, there is no guarantee that the rate of change of either the temperature or the current can be within a specific range. Therefore, to make sure that the temperature change rate is not higher than 6 °C/min, every simulation result of the PI control case should be checked. If the temperature change rate is too high, a more alleviated
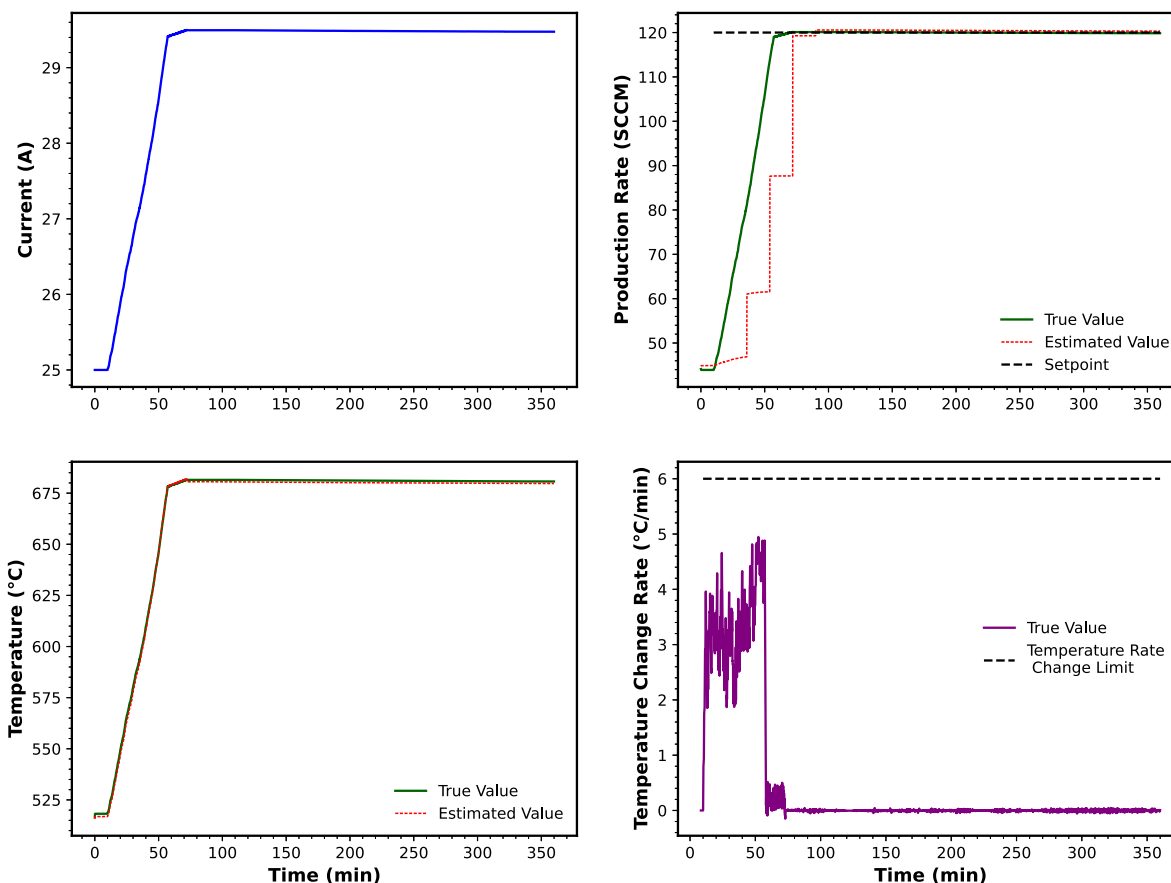
Fig. 9. Closed-loop H$_2$ production rate and control action under MPC in the presence of process variability.

PI strategy should be applied. Considering these factors, it is advisable for the PI controller to be designed with mild parameters. In our case, K_c and τ_I are tuned to be $0.00115 \frac{A}{SCCM}$ and 78 s respectively.

Remark 13. For the closed-loop system under MPC, the top-right plot of Fig. 6 displays the evolution of the H$_2$ production rate estimated by the ELO. In Eq. (17), the $F_{H_2,m}$ term is updated every 18 min. Given that the inherent observer dynamics are very fast, this new measurement results in a sudden change in the estimate occurring every 18 min. Additionally, a 15-minute measurement delay should be accounted for given that, due to the operation of the gas chromatograph, the final value of the H$_2$ production rate is similar to the true H$_2$ production rate 15 min earlier rather than true H$_2$ production rate at the current moment. During each sampling time, the observed H$_2$ production rate was almost constant since the gain of the observer error term ($K_{H_2,4}$) is large, so the dominant factor influencing the slope of the observer destination curve is the observer error term and this term is almost zero after the fast transient occurring right after the new measurement update.

5.3. Handling process variability

A key feature of any control system is its ability to counteract the impact of disturbances and process variability. Considering that coke formation on the catalyst is common in steam methane reforming systems, catalyst performance may be affected which may be modeled as a change in reaction activation energy. Therefore, in this section, a change in activation energy is utilized as a disturbance to test the robustness properties of the controller.

The impact of the disturbance is first evaluated by an open-loop simulation. In this case, the dynamic behavior of the H$_2$ production rate at a constant temperature (514 °C) is illustrated in Fig. 7. From this plot, it is evident that the H$_2$ production rate changes from 51.4 $SCCM$ to 43.2 $SCCM$ after changing the activation energy of each reaction by 2% under open-loop conditions. Therefore, the impact of this process variation on the H$_2$ production rate is significant. Fig. 7 also demonstrates that, in this new process operating condition, the time to reach the steady state is significantly shorter.

Fig. 8 displays the closed-loop results under this disturbance in the case of using a PI controller. Since the activation energy is changed, the H$_2$ production rate at the initial steady state time changes from 51.4 SCCM to 43.2 SCCM. Also, a higher value of the current (29.5 A) is needed to reach the set-point of the H$_2$ production rate, since a higher energy is required to increase the temperature of the reactor when the activation energy is higher. However, even though the condition has been changed, the H$_2$ production rate can still get to the set-point under the PI controller.

For the closed-loop simulation with MPC under this process variability scenario, it is assumed that a 2% increase in activation energy for each reaction (Eqs. (1a) and (1b)) is applied as the disturbance in the process model but this change is not implemented in the model used by the model predictive controller. Hence, the model used in MPC would not have an accurate prediction for the H$_2$ production rate. Consequently, the current obtained from the MPC would also not be able to drive the H$_2$ production rate to the set-point. To deal with this problem, an integrator term is used to add integral action into the control action calculated by the MPC. The control action u is calculated from as follows:

$$u = u_{MPC} + \frac{1}{\tau_I'} \int_0^t (F_{H_2,sp} - \hat{F}_{H_2}(\tau)) \, d\tau \tag{25a}$$

$$I = u + I_s \tag{25b}$$

where u_{MPC} is the control action calculated by the MPC, the second term in Eq. (25a) is the integrator, and I_s is the initial current value at the initial steady state. Due to this additional integrator term, the control input is expected to drive the H_2 production rate to the set-point even though the model used in the MPC is not fully capturing the actual process dynamic and steady-state behavior. The tuning of τ'_I requires to balance the constraint on the current rate of change (and thus, τ'_I cannot be too small leading to a very strong integral term) and the need to achieve offset-less set-point tracking in a practical time scale.

The closed-loop results of the MPC combined with the integrator are shown in Fig. 9. For the initial and the final steady state region, the behaviors are similar to that under the PI controller. The H_2 production rate is 43.2 SCCM when the current is 25 A and the H_2 production rate is at the set-point (120 SCCM) when the current is 29.5 A. However, during the transient, the MPC drives the H_2 production rate much faster than the PI controller to the set-point, resulting in more optimal closed-loop response while respecting all control action constraints. The bottom two plots of Fig. 9 demonstrate the simulated temperature and the simulated rate of change of temperature under the MPC. The temperature rate of change is smaller than the upper limit of the temperature change rate limit for all times.

Remark 14. For the MPC combined with the integrator control system, the constraint on the rate of change of the control action should be tighter compared to the MPC system without the integrator. This is because the control action calculated by the MPC is added to the control action calculated by the integrator term, resulting in a new control action which should satisfy the rate of change control action constraint. Therefore, the constraint on the rate of change of the control action imposed in the MPC system should be decreased compared to the case of implementing the MPC without the addition of the integrator. Furthermore, the tuning parameter for the integrator term (τ'_I) should be large enough to slightly influence the magnitude and rate of change of the overall control action.

6. Conclusion

In this study, a lumped parameter dynamic model was developed and validated against experimental data, confirming its accuracy and time efficiency in capturing the dynamic behavior of an electrically heated steam methane reforming system. The SMR system's set-point tracking control, characterized by limited, infrequent and delayed gas-phase reactor outlet measurements alongside frequent reactor temperature measurements, was effectively carried out using state estimation-based model predictive control using an extended Luenberger-type observer. The robustness of the control strategy was demonstrated specifically against process variability resulting from catalyst deactivation, a commonly encountered issue in SMR processes. The experimental implementation of the developed control strategy will be presented in a subsequent paper.

CRediT authorship contribution statement

Xiaodong Cui: Writing – original draft, Software, Methodology, Investigation, Formal analysis, Conceptualization. **Berkay Çıtmacı:** Writing – original draft, Validation, Methodology, Investigation. **Dominic Peters:** Validation, Methodology, Conceptualization. **Fahim Abdullah:** Writing – original draft, Methodology, Investigation, Conceptualization. **Yifei Wang:** Investigation, Conceptualization. **Esther Hsu:** Investigation. **Parth Chheda:** Validation, Investigation. **Carlos G. Morales-Guio:** Writing – review & editing, Investigation, Conceptualization. **Panagiotis D. Christofides:** Writing – review & editing, Supervision, Project administration, Methodology, Conceptualization.

References

Abbas, S., Dupont, V., Mahmud, T., 2017. Kinetics study and modelling of steam methane reforming process over a NiO/Al^{2}O^3 catalyst in an adiabatic packed bed reactor. Int. J. Hydrogen Energy 42 (5), 2889–2903.

Ashik, U., Daud, W.W., Abbas, H.F., 2017. Methane decomposition kinetics and reaction rate over Ni/SiO^2 nanocatalyst produced through co-precipitation cum modified Stöber method. Int. J. Hydrogen Energy 42, 938–952.

Boggs, P.T., Tolle, J.W., 1995. Sequential quadratic programming. Acta Numer. 4, 1–51.

Bowker, M., 2019. Methanol synthesis from CO^2 hydrogenation. ChemCatChem 11 (17), 4238–4246.

Christofides, P.D., Scattolini, R., de la Pena, D.M., Liu, J., 2013. Distributed model predictive control: A tutorial review and future research directions. Comput. Chem. Eng. 51, 21–41.

Çıtmacı, B., Cui, X., Abdullah, F., Richard, D., Peters, D., Wang, Y., Hsu, E., Chheda, P., Morales-Guio, C.G., Christofides, P.D., 2024. Model predictive control of an electrically-heated steam methane reformer. Digit. Chem. Eng. 10, 100138.

Dochain, D., 2003. State and parameter estimation in chemical and biochemical processes: a tutorial. J. Process Control 13, 801–818.

El-Bousiffi, M., Gunn, D., 2007. A dynamic study of steam-methane reforming. Int. J. Heat Mass Transfer 50, 723–733.

Ellis, M., Durand, H., Christofides, P.D., 2014. A tutorial review of economic model predictive control methods. J. Process Control 24, 1156–1178.

Fogler, H.S., 2020. Elements of Chemical Reaction Engineering, fifth ed. Pearson.

Ginsburg, J.M., Piña, J., El Solh, T., De Lasa, H.I., 2005. Coke formation over a nickel catalyst under methane dry reforming conditions: Thermodynamic and kinetic models. Ind. Eng. Chem. Res. 44, 4846–4854.

Guo, Y., Huang, B., 2015. State estimation incorporating infrequent, delayed and integral measurements. Automatica 58, 32–38.

Han, J., 1995. A class of extended state observers for uncertain systems. Control Decis. 10, 85–88.

Häussinger, P., Lohmüller, R., Watson, A.M., 2011. Hydrogen, 2. Production. In: Ullmann's Encyclopedia of Industrial Chemistry. John Wiley & Sons, Ltd.

Holladay, J.D., Hu, J., King, D.L., Wang, Y., 2009. An overview of hydrogen production technologies. Catal. Today 139, 244–260.

Lao, L., Aguirre, A., Tran, A., Wu, Z., Durand, H., Christofides, P.D., 2016. CFD modeling and control of a steam methane reforming reactor. Chem. Eng. Sci. 148, 78–92.

Luenberger, D., 1966. Observers for multivariable systems. IEEE Trans. Automat. Control 11, 190–197.

Mokheimer, E.M., Ibrar Hussain, M., Ahmed, S., Habib, M.A., Al-Qutub, A.A., 2015. On the modeling of steam methane reforming. J. Energy Resour. Technol. 137, 012001.

Molburg, J.C., Doctor, R.D., 2003. Hydrogen from steam-methane reforming with CO^2 capture. In: Proceedings of 20th Annual International Pittsburgh Coal Conference. Pittsburgh, PA, pp. 1–21.

Ramachandran, R., Menon, R.K., 1998. An overview of industrial uses of hydrogen. Int. J. Hydrogen Energy 23, 593–598.

Siddiqui, O., Ishaq, H., Chehade, G., Dincer, I., 2020. Experimental investigation of an integrated solar powered clean hydrogen to ammonia synthesis system. Appl. Therm. Eng. 176, 115443.

Tran, A., Aguirre, A., Durand, H., Crose, M., Christofides, P.D., 2017. CFD modeling of a industrial-scale steam methane reforming furnace. Chem. Eng. Sci. 171, 576–598.

Uddin, M.N., Nageshkar, V.V., Asmatulu, R., 2020. Improving water-splitting efficiency of water electrolysis process via highly conductive nanomaterials at lower voltages. Energy Ecol. Environ. 5, 108–117.

Wang, W., Gao, Z., 2003. A comparison study of advanced state observer design techniques. In: Proceedings of the 2003 American Control Conference. Denver, CO, pp. 4754–4759.

Wei, J., Iglesia, E., 2004a. Isotopic and kinetic assessment of the mechanism of methane reforming and decomposition reactions on supported iridium catalysts. Phys. Chem. Chem. Phys. 6, 3754–3759.

Wei, J., Iglesia, E., 2004b. Mechanism and site requirements for activation and chemical conversion of methane on supported Pt clusters and turnover rate comparisons among noble metals. J. Phys. Chem. B 108, 4094–4103.

Wei, J., Iglesia, E., 2004c. Reaction pathways and site requirements for the activation and chemical conversion of methane on ru- based catalysts. J. Phys. Chem. B 108, 7253–7262.

Wei, J., Iglesia, E., 2004d. Structural requirements and reaction pathways in methane activation and chemical conversion catalyzed by rhodium. J. Catal. 225, 116–127.

Wismann, S.T., Engbæ k, J.S., Vendelbo, S.r.B., Bendixen, F.B., Eriksen, W.L., Aasberg-Petersen, K., Frandsen, C., Chorkendorff, I., Mortensen, P.M., 2019. Electrified methane reforming: A compact approach to greener industrial hydrogen production. Science 364, 756–759.

Xu, J., Froment, G.F., 1989. Methane steam reforming, methanation and water-gas shift: I. intrinsic kinetics. AIChE J. 35, 88–96.

Yue, M., Lambert, H., Pahon, E., Roche, R., Jemei, S., Hissel, D., 2021. Hydrogen energy systems: A critical review of technologies, applications, trends and challenges. Renew. Sustain. Energy Rev. 146, 111180.

Zhang, H., Sun, Z., Hu, Y.H., 2021. Steam reforming of methane: Current states of catalyst design and process upgrading. Renew. Sustain. Energy Rev. 149, 111330.

Zhao, Q., Wang, Y., Wang, Y., Li, L., Zeng, W., Li, G., Hu, C., 2020. Steam reforming of CH_4 at low temperature on Ni/ZrO_2 catalyst: Effect of H_2O/CH_4 ratio on carbon deposition. Int. J. Hydrogen Energy 45, 14281–14292.